

A Multi-Antenna GNSS-Over-Fiber System for High Accuracy Three-Dimensional Baseline Measurement

Xin Jiang¹, Xiangchuan Wang¹, Angran Zhao, Jianping Yao², *Fellow, IEEE, Fellow, OSA*, and Shilong Pan¹, *Senior Member, IEEE, Senior Member, OSA*

Abstract—A novel multi-antenna global navigation satellite system that uses fibers to transmit signals from multiple remote antennas to a local station with real-time microwave-photonics-based fiber length monitoring is proposed for high accuracy three-dimensional (3D) baseline measurement. In the proposed approach, microwave-photonics-based fiber length monitoring is employed to obtain the delay difference between the different GNSS channels. With the obtained delay difference information, we use the carrier-phase single-difference (SD) algorithm to calculate the 3D baseline, which is able to improve the vertical precision of the 3D baseline measurement as compared with the use of the carrier-phase double-difference (DD) algorithm. Experimental results show that the 3D baseline measurement precision using the SD algorithm is within 2 mm and the vertical positioning precision is improved by over three times compared with the approach using the conventional DD algorithm.

Index Terms—Baseline, carrier phase single difference algorithm, GNSS over fiber, line bias.

I. INTRODUCTION

THE global navigation satellite system (GNSS) is widely used in applications, such as vehicle navigation and control, geophysics and geology, surveying, atmospheric exploration, and so on [1]–[3]. In most civilian applications, the GNSS based systems are usually used for single point positioning measurement with an accuracy of several meters. The GNSS can also work in the relative positioning mode, in which the carrier phase

difference of the signals received by distributed GNSS receivers is utilized to measure displacement or deflection behavior at a sub-centimeter level. This accuracy can enable the measurement of the attitude of vehicles [4], [5] and the monitoring of the healthy condition of structures such as bridges, tunnels and dams [6]–[10]. To lower the complexity and the cost caused by the multiple GNSS receivers, a multi-antenna GNSS, which consists of multiple distributed antennas and a single GNSS receiver connected by electrical cables was proposed [11]. However, in practical applications, the multi-antenna GNSS faces at least two problems. First, deformation monitoring in a wide area requires stable long-distance transmission of the GNSS signals, while the electrical cables are usually lossy. In addition, there lack convenient methods for real-time delay measurement of the electrical cable. Second, as GNSS satellites are only visible above the local horizon, distribution of the satellites is uniform and symmetrical in the horizontal directions but asymmetrical in the vertical direction, leading to a poor vertical measurement accuracy, which is 2 or 3 times worse than that of the horizontal one [12]. This problem directly affects the applications requiring the vertical displacement monitoring.

To solve the long-distance transmission problem, the radio-over-fiber technique is proposed and considered an effective method. Previously, a GPS-over-fiber system was constructed for aircraft attitude determination [13], [14], which applied optical fiber for the transmission of differential GPS signals. To solve the problem of low vertical component accuracy, adopting the carrier phase SD model rather than the conventional carrier phase DD model is a potential method [15]. The conventional DD model can be obtained by making another difference between two satellites based on the SD model. Although the conventional DD model between satellites can be utilized to eliminate the errors due to the receiver's clock bias and the line bias, the observational noise of the DD model is $\sqrt{2}$ as much as that of the SD model [16]. The concept of a multi-antenna receiver was proposed, with 2 times improvement of the vertical accuracy achieved by simulation analysis in [17] and experimental demonstration in [15]. In addition, the carrier phase SD algorithm has several other advantages comparing with the carrier phase DD algorithm. First, the SD algorithm can be applied for different types of the GNSS. For example, the combination of GPS and GLONASS was realized by using the carrier phase SD

Manuscript received February 22, 2019; revised April 30, 2019; accepted June 5, 2019. Date of publication June 10, 2019; date of current version August 8, 2019. This work was supported in part by the National Natural Science Foundation of China (61605077 and 61527820), in part by the Jiangsu Provincial “333” Project (BRA2018042), in part by the Fundamental Research Funds for the Central Universities (NT2019011), and in part by the Young Elite Scientists Sponsorship Program by CAST (2018QNRC001). (*Corresponding authors: Xiangchuan Wang and Shilong Pan.*)

X. Jiang, X. Wang, A. Zhao, and S. Pan are with the Key Laboratory of Radar Imaging and Microwave Photonics, Ministry of Education, Nanjing University of Aeronautics and Astronautics, Nanjing 210016, China (e-mail: jiangx@nuaa.edu.cn; wangxch@nuaa.edu.cn; zhaoangran@nuaa.edu.cn; pans@ieee.org).

J. Yao is with the Microwave Photonics Research Laboratory, School of Electrical Engineering and Computer Science, University of Ottawa, Ottawa, ON K1N 6N5, Canada (e-mail: jpyao@uottawa.ca).

Color versions of one or more of the figures in this paper are available online at <http://ieeexplore.ieee.org>.

Digital Object Identifier 10.1109/JLT.2019.2921865

algorithm [18]. Second, higher success rate of integer ambiguity resolution can be realized by the carrier phase SD algorithm [19].

In the carrier phase SD algorithm, line bias, which denotes the different time delays of signal paths between the antennas and the receiver is a very important parameter [20]. Since it will vary with time due to the temperature variation and mechanical forces in the environment, real-time line bias monitoring should be realized in order to improve the positioning precision of the vertical component. In [15], cables are made equal in length to minimize the line bias variation. However, considerable errors could still exist if the temperature and mechanical force are not uniform in the area to be monitored. To solve this problem, a GPS-over-fiber scheme with line bias monitoring using two optical fibers in one cable is proposed [21]. However, the measurement of the line bias is accurate only when the two optical fiber lengths change synchronously, which is not the case in practical application. We have proposed a multi-antenna GNSS-over-fiber architecture based on radio-over-fiber and microwave-photonics-based line bias monitoring techniques [22]. The proposed method have several advantages. Firstly, a radio-over-fiber technique is proposed to reduce power transmission loss in the conventional cable-connected distributed GNSS. Secondly, a microwave-photonics-based fiber length monitoring structure realized the real-time and high-precision line bias parameter measurement. Thirdly, the carrier phase SD algorithm with line bias compensation is utilized to improve the vertical positioning precision in the GNSS. But only some preliminary results were reported, which was insufficient to understand the approach in-depth.

In this manuscript, we perform a comprehensive theoretical and experimental study of the GNSS-over-fiber system with real-time microwave-photonics-based fiber length monitoring. In Section II, an analytical model to reveal the impact of the line bias monitoring on the 3D baseline measurement is established, and the operational principle of the proposed multi-antenna GNSS-over-fiber system is introduced. In Section III, an experiment is carried out, which shows that the 3D baseline measurement precision using the SD algorithm is within 2 mm, and the vertical positioning precision is improved by over 3 times compared with the case using the conventional DD algorithm. A conclusion is drawn in Section IV.

II. PRINCIPLE

A. Carrier Phase SD Algorithm With Line Bias Compensation

The model of the GPS signal carrier phase measurement is shown in Fig. 1. The carrier phase measurement can be written as [23]

$$\lambda\phi_i^k = \rho_i^k - I_i^k + T_i^k + c(\delta t_i - \delta t^k) + LB_i + \lambda N_i^k + e_i \quad (1)$$

where λ represents the wavelength of the carrier, ϕ_i^k denotes the measured carrier phase, k is the satellite's number, i is the antenna's number, ρ_i^k represents the geometric range between the i th antenna and the k th satellite, I and T are the ionosphere and tropospheric delay, c denotes the light speed in vacuum, δt represents the clock error, LB_i represents the line bias between

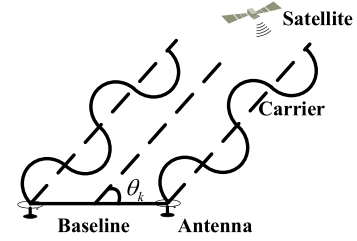


Fig. 1. The model of the GPS signal carrier phase measurement.

the receiver and the antenna, N_i^k is the integer ambiguity, and e_i is the observational noise.

The SD model can be obtained by making a difference of the measured carrier phases from two antennas,

$$\lambda\Delta\phi_{ij}^k = \Delta\rho_{ij}^k + c\Delta\delta t_{ij} + \Delta LB_{ij} + \lambda\Delta N_{ij}^k + \Delta e_{ij} \quad (2)$$

where Δ is the SD operation. As can be seen, the ionosphere delay, tropospheric delay, and the satellite's clock bias are eliminated by the SD operation.

Considering that the length of the baseline is much smaller than the distance from a satellite to an antenna, so $\Delta\rho_{ij}^k$ can be expressed as

$$\Delta\rho_{ij}^k \approx |\mathbf{b}| \cos \theta_k = \mathbf{s}^k \mathbf{b}^T \quad (3)$$

where $\mathbf{b} = [b_x \ b_y \ b_z]$ is the baseline vector, $\mathbf{s}^k = [s_x^k \ s_y^k \ s_z^k]$ is the normalized line of sight vector to the k th satellite, \mathbf{b}^T is the transposed matrix of \mathbf{b} .

Then (2) can be rewritten by

$$\lambda\Delta\phi_{ij}^k = \mathbf{s}^k \mathbf{b}^T + c\Delta\delta t_{ij} + \Delta LB_{ij} + \lambda\Delta N_{ij}^k + \Delta e_{ij} \quad (4)$$

When a multi-antenna GNSS receiver with one same common clock reference source is used, the receiver's clock bias is eliminated, i.e.,

$$\Delta\delta t_{ij} = \delta t_i - \delta t_j = 0 \quad (5)$$

Suppose n satellites are tracked, The SD model can be expressed as

$$\lambda \begin{bmatrix} \Delta\phi_{ij}^1 \\ \Delta\phi_{ij}^2 \\ \dots \\ \Delta\phi_{ij}^n \end{bmatrix}_{n \times 1} = \begin{bmatrix} \mathbf{s}^1 \\ \mathbf{s}^2 \\ \dots \\ \mathbf{s}^n \end{bmatrix} \mathbf{b}^T + \begin{bmatrix} 1 \\ 1 \\ \dots \\ 1 \end{bmatrix} \Delta LB_{ij} + \lambda \begin{bmatrix} \Delta N_{ij}^1 \\ \Delta N_{ij}^2 \\ \dots \\ \Delta N_{ij}^n \end{bmatrix}_{n \times 1} + \begin{bmatrix} \Delta e_{ij}^1 \\ \Delta e_{ij}^2 \\ \dots \\ \Delta e_{ij}^n \end{bmatrix} \quad (6)$$

At the local station, the carrier phase ϕ_i^k can be directly measured. Thus the vector in the left hand of (6) can be derived. The rough locations of the satellites and the antennas can be obtained by pseudorange and ephemeris after parsing the observation data, so the normalized line of sight vector \mathbf{s}^k can also be achieved. The SD integer ambiguity ΔN_{ij}^k can be calibrated in advance by using the long-time average-filtering DD solution [24]. The real-time line bias ΔLB_{ij} equals to the initial

line bias plus the line bias compensation parameter. The former can be measured via the long-time average-filtering DD solution [24], while the latter is achieved in this work by using the proposed microwave-photonics-based fiber length monitoring. With the known $\Delta\phi_{ij}^k$, s^k , ΔLB_{ij} and ΔN_{ij}^k , the baseline \mathbf{b} can be obtained by the least square method.

B. The Impact of the Line Bias Measurement Accuracy on the Baseline Measurement Accuracy

To investigate the impact of the line bias measurement accuracy on the baseline measurement accuracy, the SD model with line bias compensation can be rewritten as

$$\begin{aligned} \begin{bmatrix} \lambda\Delta\phi_{ij}^1 - \Delta LB_{ij} \\ \lambda\Delta\phi_{ij}^2 - \Delta LB_{ij} \\ \dots \\ \lambda\Delta\phi_{ij}^n - \Delta LB_{ij} \end{bmatrix}_{n \times 1} &= \begin{bmatrix} \mathbf{s}^1 \\ \mathbf{s}^2 \\ \dots \\ \mathbf{s}^n \end{bmatrix} \mathbf{b}^T + \begin{bmatrix} 1 \\ 1 \\ \dots \\ 1 \end{bmatrix} \delta\Delta LB_{ij} \\ &+ \lambda \begin{bmatrix} \Delta N_{ij}^1 \\ \Delta N_{ij}^2 \\ \dots \\ \Delta N_{ij}^n \end{bmatrix}_{n \times 1} \end{aligned} \quad (7)$$

The left of (7) is the measured parameters consisting of the carrier phase and the line bias while the right parts are the parameters consisting of the baseline vector to be calculated, the calibration error of the initial line bias $\delta\Delta LB_{ij}$ and the SD integer ambiguity.

For simplicity, new parameters \mathbf{Y}_Δ and \mathbf{S} are defined,

$$\mathbf{Y}_\Delta = \begin{bmatrix} \lambda\Delta\phi_{ij}^1 - \Delta LB_{ij} \\ \lambda\Delta\phi_{ij}^2 - \Delta LB_{ij} \\ \dots \\ \lambda\Delta\phi_{ij}^n - \Delta LB_{ij} \end{bmatrix}_{n \times 1} \quad (8)$$

$$\mathbf{S} = \begin{bmatrix} \mathbf{s}^1 \\ \mathbf{s}^2 \\ \dots \\ \mathbf{s}^n \end{bmatrix} = \begin{bmatrix} s_x^1 & s_y^1 & s_z^1 \\ s_x^2 & s_y^2 & s_z^2 \\ \dots & \dots & \dots \\ s_x^n & s_y^n & s_z^n \end{bmatrix} \quad (9)$$

so (7) can be rewritten as:

$$\mathbf{Y}_\Delta = [\mathbf{S}|\mathbf{e}_n] \begin{bmatrix} \mathbf{b}^T \\ \delta\Delta LB_{ij} \end{bmatrix} + \lambda \begin{bmatrix} \Delta N_{ij}^1 \\ \Delta N_{ij}^2 \\ \dots \\ \Delta N_{ij}^n \end{bmatrix}_{n \times 1} = \mathbf{B}\mathbf{X} + \mathbf{C}\mathbf{N} \quad (10)$$

where $\mathbf{e}_n = [1 \ 1 \ \dots]^T$, $\mathbf{B} = [\mathbf{S}|\mathbf{e}_n]$, $\mathbf{X} = [\mathbf{b}^T \ \delta\Delta LB_{ij}]^T$, $\mathbf{C} = \lambda\mathbf{I}_n$, and $\mathbf{N} = [\Delta N_{ij}^1 \ \Delta N_{ij}^2 \ \dots \ \Delta N_{ij}^n]^T$.

To get the variance-covariance matrix of \mathbf{Y}_Δ , (8) is modified,

$$\mathbf{Y}_\Delta = \lambda \begin{bmatrix} \Delta\phi_{ij}^1 \\ \Delta\phi_{ij}^2 \\ \dots \\ \Delta\phi_{ij}^n \end{bmatrix}_{n \times 1} - \mathbf{I}\Delta LB_{ij} = \mathbf{G} \begin{bmatrix} \phi_j^1 \\ \phi_i^1 \\ \phi_j^2 \\ \phi_i^2 \\ \dots \\ \phi_j^n \\ \phi_i^n \end{bmatrix}_{2n \times 1} - \mathbf{I}\Delta LB_{ij} \quad (11)$$

where

$$\mathbf{G} = \begin{bmatrix} 1 & -1 & 0 & 0 & \dots & 0 & 0 \\ 0 & 0 & 1 & -1 & \dots & 0 & 0 \\ & & & & \dots & & \\ 0 & 0 & 0 & 0 & \dots & 1 & -1 \end{bmatrix} \quad (12)$$

Suppose that the precision of the carrier phase (ϕ_j^k) measurement and the line bias (ΔLB_{ij}) measurement are σ_ϕ^2 and $\sigma_{\Delta LB_{ij}}^2$, the variance-covariance matrix of the carrier phase can be obtained,

$$[\phi_j^1 \ \phi_i^1 \ \phi_j^2 \ \phi_i^2 \ \dots \ \phi_j^n \ \phi_i^n]^T \sim \mathbf{I}_n \sigma_\phi^2 \quad (13)$$

According to (11)–(13) and the variance-covariance propagation law, the variance-covariance matrix of \mathbf{Y}_Δ can be expressed as

$$\begin{aligned} \mathbf{Q}_{\mathbf{Y}_\Delta} &= \mathbf{G}(\mathbf{I}_n \sigma_\phi^2) \mathbf{G}^T + \sigma_{\Delta LB_{ij}}^2 \mathbf{I}_n = 2\sigma_\phi^2 \lambda \mathbf{I}_n + \sigma_{\Delta LB_{ij}}^2 \mathbf{I}_n \\ &= (2\sigma_\phi^2 \lambda + \sigma_{\Delta LB_{ij}}^2) \mathbf{I}_n \end{aligned} \quad (14)$$

According to (10), (14) and the variance-covariance propagation law, the variance-covariance of the parameter \mathbf{X} can be obtained [25]

$$\begin{aligned} \mathbf{Q}_{\mathbf{X}} &= (\mathbf{B}^T \mathbf{Q}_{\mathbf{Y}_\Delta}^{-1} \mathbf{B})^{-1} = \left(\frac{1}{2\sigma_\phi^2 \lambda + \sigma_{\Delta LB_{ij}}^2} [\mathbf{S}|\mathbf{e}_n]^T [\mathbf{S}|\mathbf{e}_n] \right)^{-1} \\ &= (2\sigma_\phi^2 \lambda + \sigma_{\Delta LB_{ij}}^2) \begin{pmatrix} \mathbf{S}^T \mathbf{S} & \mathbf{S}^T \mathbf{e}_n \\ \mathbf{e}_n^T \mathbf{S} & \mathbf{e}_n^T \mathbf{e}_n \end{pmatrix}^{-1} \\ &= \begin{pmatrix} \mathbf{Q}_{\mathbf{b}} & \mathbf{Q}_{\mathbf{b}, \Delta LB_{ij}} \\ \mathbf{Q}_{\Delta LB_{ij}, \mathbf{b}} & \mathbf{Q}_{\Delta LB_{ij}} \end{pmatrix} \end{aligned} \quad (15)$$

By calculating the inversion of the block matrix, the variance-covariance of the baseline vector \mathbf{b} can be given by

$$\begin{aligned} \mathbf{Q}_{\mathbf{b}} &= (2\sigma_\phi^2 \lambda + \sigma_{\Delta LB_{ij}}^2) \left(\mathbf{S}^T \mathbf{S} - \mathbf{S}^T \mathbf{e}_n (\mathbf{e}_n^T \mathbf{e}_n)^{-1} \mathbf{e}_n^T \mathbf{S} \right)^{-1} \\ &= (2\sigma_\phi^2 \lambda + \sigma_{\Delta LB_{ij}}^2) \left(\mathbf{S}^T \mathbf{S} - \frac{1}{n} \mathbf{S}^T \mathbf{e}_n \mathbf{e}_n^T \mathbf{S} \right)^{-1} \\ &= (2\sigma_\phi^2 \lambda + \sigma_{\Delta LB_{ij}}^2) \left(\mathbf{S}^T \mathbf{S} - \frac{1}{\sqrt{n}} \mathbf{S}^T \mathbf{e}_n \times \frac{1}{\sqrt{n}} \mathbf{e}_n^T \mathbf{S} \right)^{-1} \end{aligned} \quad (16)$$

To simplify the second part of (16), we expand the inverse matrix [26] as

$$(\mathbf{A} - \mathbf{a}\mathbf{a}^T)^{-1} = \mathbf{A}^{-1} + \frac{1}{1 - \mathbf{a}^T\mathbf{A}^{-1}\mathbf{a}}\mathbf{A}^{-1}\mathbf{a}\mathbf{a}^T\mathbf{A}^{-1} \quad (17)$$

$\mathbf{a} = \frac{1}{\sqrt{n}}\mathbf{S}^T\mathbf{e}_n$ and $\mathbf{A} = \mathbf{S}^T\mathbf{S}$ which is a symmetric matrix are also defined, so we obtain

$$\mathbf{A}^{-1}\mathbf{a}\mathbf{a}^T\mathbf{A}^{-1} = \mathbf{A}^{-1}\mathbf{a}(\mathbf{A}^{-1}\mathbf{a})^T \quad (18)$$

With (17) and (18), the second part of (16) can be expanded as

$$\begin{aligned} & \left(\mathbf{S}^T\mathbf{S} - \frac{1}{\sqrt{n}}\mathbf{S}^T\mathbf{e}_n \times \frac{1}{\sqrt{n}}\mathbf{e}_n^T\mathbf{S} \right)^{-1} = (\mathbf{S}^T\mathbf{S})^{-1} \\ & + \frac{1}{1 - \frac{1}{n}\mathbf{e}_n^T\mathbf{S}(\mathbf{S}^T\mathbf{S})^{-1}\mathbf{S}^T\mathbf{e}_n} \\ & \times \frac{1}{n}(\mathbf{S}^T\mathbf{S})^{-1}\mathbf{S}^T\mathbf{e}_n \left[(\mathbf{S}^T\mathbf{S})^{-1}\mathbf{S}^T\mathbf{e}_n \right]^T \end{aligned} \quad (19)$$

To simplify the second part of (19), we define the orthogonal projection matrix of \mathbf{S} as \mathbf{P}_s and let

$$\mathbf{P}_s = \mathbf{S}(\mathbf{S}^T\mathbf{S})^{-1}\mathbf{S}^T \quad (20)$$

$$\mathbf{F}_s = (\mathbf{S}^T\mathbf{S})^{-1}\mathbf{S}^T \quad (21)$$

$$\sigma^2 = 2\sigma_\phi^2\lambda + \sigma_{\Delta L B_{ij}}^2 \quad (22)$$

With (19)–(22), (16) can be simplified as

$$\mathbf{Q}_b = \sigma^2 \left[(\mathbf{S}^T\mathbf{S})^{-1} + \frac{1}{n - (\mathbf{P}_s\mathbf{e}_n)^T\mathbf{P}_s\mathbf{e}_n} \mathbf{F}_s\mathbf{e}_n(\mathbf{F}_s\mathbf{e}_n)^T \right] \quad (23)$$

To simplify the second part of (23), considering that the length of a vector is larger than the length of its projection, so we let

$$p = n - (\mathbf{P}_s\mathbf{e}_n)^T\mathbf{P}_s\mathbf{e}_n = \|\mathbf{e}_n\| - \|\mathbf{P}_s\mathbf{e}_n\| > 0 \quad (24)$$

$$\mathbf{F}_s\mathbf{e}_n = (\mathbf{S}^T\mathbf{S})^{-1}\mathbf{S}^T\mathbf{e}_n$$

$$\begin{aligned} & \begin{pmatrix} \sum_{i=1}^n (s_x^i)^2 & \sum_{i=1}^n s_x^i s_y^i & \sum_{i=1}^n s_x^i s_z^i \\ \sum_{i=1}^n s_y^i s_x^i & \sum_{i=1}^n (s_y^i)^2 & \sum_{i=1}^n s_y^i s_z^i \\ \sum_{i=1}^n s_z^i s_x^i & \sum_{i=1}^n s_z^i s_y^i & \sum_{i=1}^n (s_z^i)^2 \end{pmatrix}^{-1} \begin{pmatrix} \sum_{i=1}^n s_x^i \\ \sum_{i=1}^n s_y^i \\ \sum_{i=1}^n s_z^i \end{pmatrix} \\ & = (\mathbf{F}_x \ \mathbf{F}_y \ \mathbf{F}_z)^T \end{aligned} \quad (25)$$

To analyze (25), the following considerations should be taken into account. Due to the independence of the satellites, we have

$$\begin{cases} \lim_{n \rightarrow \infty} \left(\sum_{i=1}^n s_x^i s_y^i \right) = 0 \\ \lim_{n \rightarrow \infty} \left(\sum_{i=1}^n s_x^i s_z^i \right) = 0 \\ \lim_{n \rightarrow \infty} \left(\sum_{i=1}^n s_y^i s_z^i \right) = 0 \end{cases} \quad (26)$$

Due to the limitations of the observable satellite distribution, only the signals from GNSS satellites above the local horizon can be attainable by the receiver. Ideally, distribution of the satellites

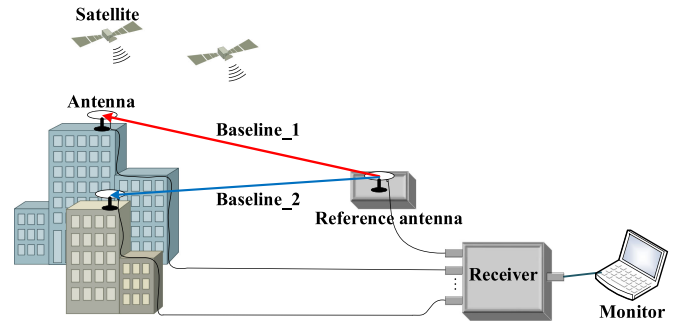


Fig. 2. The application scenario of a GNSS-based deformation monitoring system.

is uniform and symmetrical in the horizontal x and y directions while asymmetrical in the vertical z -direction, so we also have

$$\begin{cases} \lim_{n \rightarrow \infty} \left(\sum_{i=1}^n s_x^i \right) = 0 \\ \lim_{n \rightarrow \infty} \left(\sum_{i=1}^n s_y^i \right) = 0 \end{cases} \quad (27)$$

and $\sum_{i=1}^n s_z^i$ will continuously increase or decrease with n . With (26) and (27), we have $F_z \gg F_x$, $F_z \gg F_y$. Meanwhile $F_x F_y$, $F_x F_z$ and $F_z F_y$ are close to zero.

With (24) and (25), (23) can be rewritten as

$$\begin{aligned} \mathbf{Q}_b &= \sigma^2 \left[\mathbf{A}^{-1} + \frac{1}{p} (\mathbf{F}_x \ \mathbf{F}_y \ \mathbf{F}_z)^T (\mathbf{F}_x \ \mathbf{F}_y \ \mathbf{F}_z) \right] \\ &= \sigma^2 \left[\mathbf{A}^{-1} + \frac{1}{p} \begin{pmatrix} F_x^2 & F_x F_y & F_x F_z \\ F_y F_x & F_y^2 & F_y F_z \\ F_z F_x & F_z F_y & F_z^2 \end{pmatrix} \right] \end{aligned} \quad (28)$$

In (28), \mathbf{A}^{-1} and $\frac{1}{p}$ are constant, $F_z^2 \gg F_x^2$ and $F_z^2 \gg F_y^2$, $F_x F_y$, $F_x F_z$ and $F_z F_y$ are close to zero. Therefore, the z -direction component of the measured baseline is more sensitive to the total measurement errors of the carrier phase and the line bias σ^2 , indicating that accurate determination of the line bias is of great importance for the improvement of the vertical baseline precision.

C. The Proposed Multi-Antenna GNSS-Over-Fiber System

Fig. 2 shows a typical application scenario of the multi-antenna GNSS-based deformation monitoring system. One of the antennas is fixed on a rigid platform as the reference antenna, and other antennas are installed at the places that need to be monitored. The displacement can be monitored by calculating the different baselines between the fixed reference antenna and the remote antennas.

Fig. 3 shows the schematic diagram of the proposed multi-antenna GNSS-over-fiber system. The proposed system consists of GNSS-over-fiber transmission links, the real-time line bias monitoring modules and a local processing unit. At the remote site, GNSS signals are tracked by distributed antennas, then they are converted into optical signals with a Mach-Zehnder modulator (MZM) and a laser diode (LD). As compared with the directly-modulated link used in [21], the external modulated

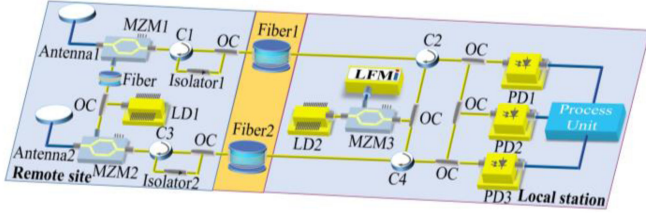


Fig. 3. Schematic diagram of the proposed multi-antenna GNSS-over-fiber system. OC: optical coupler; LD: laser diode; PD: photodetector; MZM: Mach-Zehnder modulator; C: circulator; LFM: linearly frequency-modulated signal.

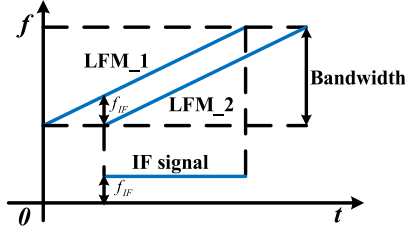


Fig. 4. Principle of the real-time microwave-photonics-based fiber length monitoring.

link in the proposed system has a lower noise floor [27], leading to a higher sensitivity of the system. The optical signals are transmitted to the local processing center via optical fibers. At last, the signals are detected by photodetectors (PDs) and parsed by a multi-channel receiver. In our experiment, remote GNSS antennas are close to each other, it is easy to connect MZM1 and MZM2 with LD1. However, in practical application as shown in Fig. 2, antennas are far from each other, an additional long fiber should be needed.

At the local station, an optical carrier from another LD is modulated by a linear frequency modulated (LFM) signal, which is split into multiple transmission links as the line bias monitoring signal. The optical monitoring signal is inserted into the transmission channel through an optical circulator and transmitted to the remote site. With an optical circulator, an optical isolator and an optical coupler (OC) at the remote site, the optical monitoring signal is reflected back to the local processing center.

The frequency of the LFM signal can be expressed as:

$$f_s = f_0 + \frac{B}{T_0}t \quad (29)$$

where f_0 is the initial frequency, T_0 and B are the duration and bandwidth of the LFM signal. If the transmission delay of the SMF1 is τ_1 , and the monitoring signal undergoes a round trip so the time delay should be $2\tau_1$. The frequency of the detected signal is expressed as:

$$f_{b1} = f_0 + \frac{B}{T_0}(t - 2\tau_1) \quad (30)$$

In our experiment, as can be seen in Fig. 4, two of the reflected LFM signals are mixed, which can generate an intermediate frequency (IF) signal. The frequency of the IF signal can be written as:

$$f_{IF} = f_{b1} - f_{b2}$$

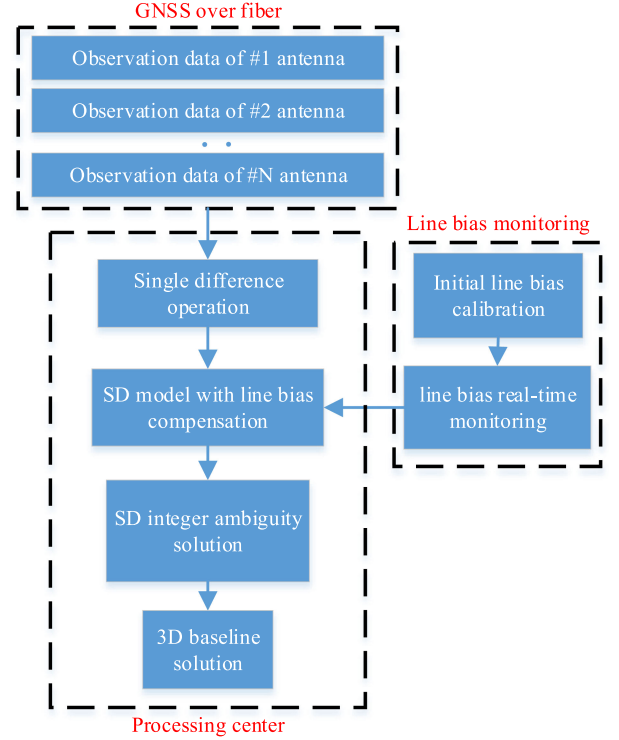


Fig. 5. Flowchart of the proposed SD algorithm with line bias compensation.

$$\begin{aligned} &= \frac{2B}{T_0}(\tau_2 - \tau_1) \\ &= \frac{2nB}{T_0} \left(\frac{L_2 - L_1}{c} \right) \end{aligned} \quad (31)$$

where L is the length of the fiber, n represents the refractive index of the optical fiber. The IF signal is proportional to the length difference of the two optical fibers which is used to calculate the line bias parameter.

In a typical bidirectional optical communication system, signals transmitted in two directions have the same signal structure. Such system is intrinsically sensitive to crosstalk from reflections and Rayleigh backscattering, since the crosstalk is directly coupled to the receiver. However, in our system, the GNSS signal and LFM signal are totally different in the signal type and power. On the one hand, the power of the received GNSS signal is ~ -130 dBm, which is much lower than that of the LFM signal. Therefore, the GNSS signal can hardly affect the monitoring signal. On the other hand, the LFM signal is a frequency-varying signal with a certain cycle, yet the frequency of the GPS L1 signal is a narrowband signal with certain center frequency of 1.57542 GHz. The narrow-band electrified filter in the GNSS receiver can filter the LFM signal well. Therefore, the LFM signal will not affect the GNSS receiver track the GNSS signal.

Fig. 5 shows the flowchart of the proposed SD algorithm with line bias compensation. The observation data of the remote antennas are transmitted to the local station by optical fibers. At the processing center, the IF signals are obtained by the proposed scheme in Fig. 3 and further translated to the line bias parameter. Then the SD algorithm with line bias compensation in (6) can be established by using the observation data and the line bias

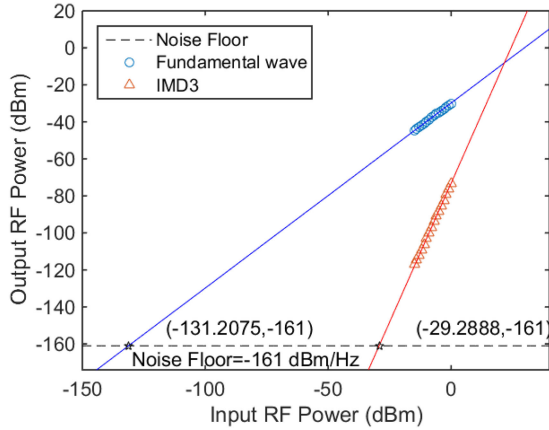


Fig. 6. Output RF power as a function of the input RF power of the external modulation based APL.

parameter. Finally, the 3D baseline can be obtained with fixed inter ambiguities.

III. EXPERIMENT RESULTS AND DISCUSSION

A proof-of-concept experiment is carried out based on the configuration shown in Fig. 3. An external modulation based analog photonic link (APL) is established for GNSS signal transmission. A lightwave at 1550.55 nm is generated from a laser source (TeraXion) with an output power of 17 dBm and split into two GNSS-over-fiber links by a 50:50 optical coupler. An MZM (Lucent 2623NA) with a bandwidth of 10 GHz and a PD with a bandwidth of 10 GHz, a responsivity of 0.65 A/W and a sensitivity of -19 dBm are used for electrical-to-optical and optical-to-electrical conversion, respectively. The electrical spectrum is measured by a 40-GHz electrical spectrum analyzer (ESA, Agilent E4447AU).

A. The Performance of the GNSS-Over-Fiber Link

To investigate the performance of the GNSS-over-fiber link, a two-tone RF signal is introduced to the APL. The frequencies of the two-tone RF signal are 1574 MHz and 1576 MHz GHz which are close to GNSS L1 carrier frequency (1575.42 MHz). The gain of the APL is -29.8 dB, which can be obtained from the relationship between the input and output power of the two-tone RF signal, as illustrated in Fig. 6.

One of the key parameters that need to be noted is the noise figure of the APL. In our implementation, the noise floor is -161 dBm/Hz by taking into account three main noise sources in the APL, including thermal noise, shot noise, and relative intensity noise [28]. Table I shows the nominal sensitivity performance of several well-known GNSS receiver chips. Considering that the noise floor of the APL is lower than the sensitivities of most GNSS receiver chips, such extra APL will not degrade the sensitivity of the whole system. On the other hand, due to the high spurious-free dynamic range (SFDR) of the APL (from -131.2 to -29.3 dBm), the weak GNSS signal with a received power of ~ -130 dBm can be easily delivered to the processing center after a low noise amplifier with low power consumption.

TABLE I
SENSITIVITIES OF DIFFERENT GNSS CHIPS

GNSS chip	Cold boot sensitivity (dBm)	Tracking sensitivity (dBm)
<i>SiRF GSC3f(e)/LP</i>	-142	-159
<i>Atmel ANTARIS4</i>	-142	-158
<i>uNav Orion</i>	-144	-160
<i>GloNav</i>	-144	-159

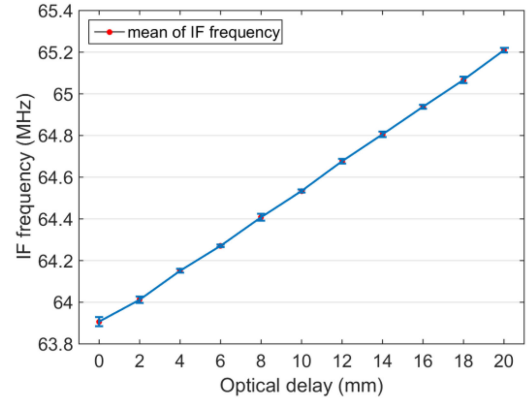


Fig. 7. The IF frequency as a function of the optical delay.

B. The Performance of the Line Bias Monitoring Module

In the line bias monitoring module at the local station, an arbitrary waveform generator (AWG, Keysight M8195A) generates a 20-GHz LFM signal. A high sensitivity PD (Thorlabs PDB450C-AC) with a bandwidth of 150 MHz and a conversion gain of 10^3 V/A is utilized to detect the IF signal. In the experiment, the initial length difference between the two optical fibers generates an IF frequency of ~ 63.9070 MHz. A variable optical delay line (VODL) is adjusted to introduce the variation of the line bias. The IF frequency is recorded while the VODL changes from 0 to 20 mm by a step of 2 mm. Fig. 7 shows the dependency relation between the IF frequency and the optical delay. A linear curve is obtained with a slope of ~ 0.065 MHz/mm. The measurement results maintain great consistency.

To analyze the factors that affect the line bias measurement precision, we write the measurement error of the fiber length difference δL as

$$\delta L = \frac{cT_0}{2nB} \delta f_{IF} \quad (32)$$

where δf_{IF} represents the frequency measurement error of the IF signal. From (32), the accuracy of the line bias is determined by the frequency measurement error of the IF signal and the bandwidth of the LFM signal. In addition, the linewidth of the IF signal would be enlarged because of the limited degree of linearity of the LFM signal, leading to further measurement errors of the line bias. Based on the error bar in Fig. 7, the maximal standard deviation (STD) of the IF frequency measurement is ~ 0.022 MHz, indicating that the precision of the line bias measurement using the proposed system is ~ 0.338 mm. To improve the precision of the line bias measurement, an LFM signal with better linearity and a wider bandwidth can be used.

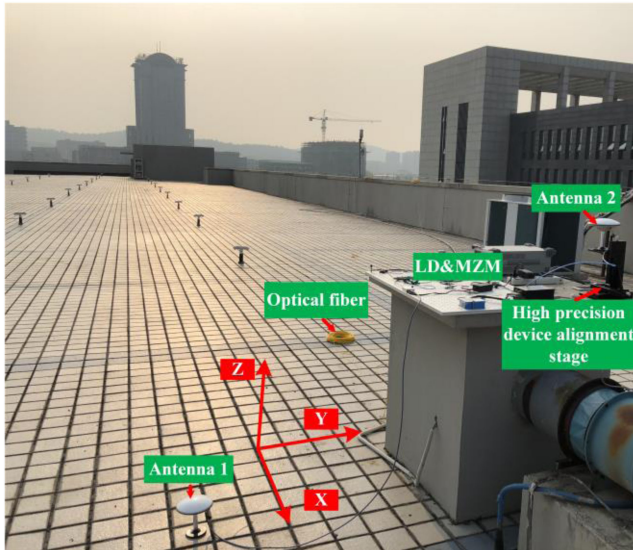


Fig. 8. The experiment setup for the outdoor measurement.



Fig. 9. The three-dimensional high precision device alignment stage used to emulate the building vibration.

C. The Measurement Accuracy of the Proposed GNSS-Over-Fiber System

Outdoor experiments are carried out based on the schematic diagram shown in Fig. 3 to verify the precision improvement by using the proposed system. As shown in Fig. 8, the remote site is set on the roof of our laboratory building to provide an unshielded observation environment for the 3D baseline measurement. Two 200-meter-long single-mode optical fibers are utilized as the transmission link between the remote site and the local station. The processing unit and the line bias monitoring module are placed in the laboratory. The processing unit consists of a multichannel receiver for GNSS signal processing and a computer for the carrier phase SD algorithm with line bias compensation.

A three-dimensional high precision device alignment stage is employed to emulate the building vibration, as shown in Fig. 9. To obtain the measurement precision of the three directions of the baseline, the alignment stage is moved by $50 \text{ mm} \times 2$ in

TABLE II
X-AXIS MEASUREMENT RESULTS

Stage	STD of DD (mm)	Displacement ΔX of DD (mm)	STD of SD (mm)	Displacement ΔX of SD (mm)
1	1.4	null	1.4	null
2	1.2	50.9	1.3	47.2
3	1.2	51.8	1.6	53.1

TABLE III
Y-AXIS MEASUREMENT RESULTS

Stage	STD of DD (mm)	Displacement ΔY of DD (mm)	STD of SD (mm)	Displacement ΔY of SD (mm)
1	1.9	null	1.6	null
2	1.3	52.4	1.0	49.7
3	1.2	47.9	1.6	51.8

TABLE IV
Z-AXIS MEASUREMENT RESULTS

Stage	STD of DD (mm)	Displacement ΔZ of DD (mm)	STD of SD (mm)	Displacement ΔZ of SD (mm)
1	3.3	null	1.0	null
2	8.3	53.3	1.2	48.7
3	4.8	41.9	1.1	49.0

each of the three directions. Fig. 10 shows the 3D baseline measurement results of the SD model using the proposed system and the conventional DD model, and Tables II, III and IV compare the STD and the displacement of the three components achieved by the two models. Table II shows the x-axis statistical result of the device moving along the x-axis. Table III shows the y-axis statistical result of the device moving along the y-axis. Table II shows the z-axis statistical result of the device moving along the z-axis. Fig. 10(a) and (b) represent the baseline measurement results of the horizontal displacement. From Tables II and III, it can be found that the precision of the x and y components of the SD model during the three stages are all below 2 mm, which is very close to those achieved by the DD model. However, the precision of the z component is improved from 6.9 mm by the DD model to 1.2 mm by the SD model as seen in the z-axis result of Fig. 10(a), and from 12.8 mm by the DD model to 2.7 mm by the SD model as seen in the z-axis result of Fig. 10(b), indicating improvements of 5.75 and 4.74 times, respectively. Regarding the vertical component during the three stages, the SD model still provides a measurement precision of less than 2 mm, while that obtained by the DD model is over 3 mm. As can be seen in Table IV, the precision of the vertical component is improved from 3.3 mm by the DD model to 1.0 mm by the SD model in Stage 1, from 8.3 mm by the DD model to 1.2 mm by the SD model in Stage 2 and from 4.8 mm by the DD model to 1.1 mm by the SD model in Stage 3, indicating improvements of 3.30, 6.92 and 4.36 times, respectively. For the displacement measurements, the SD model has errors of 1.3 mm and 1.0 mm while those obtained by the DD model are 3.3 mm and 8.1 mm.

These experimental results show that the vertical positioning precision can be greatly improved by using the proposed method, while the horizontal positioning precision is not reduced.

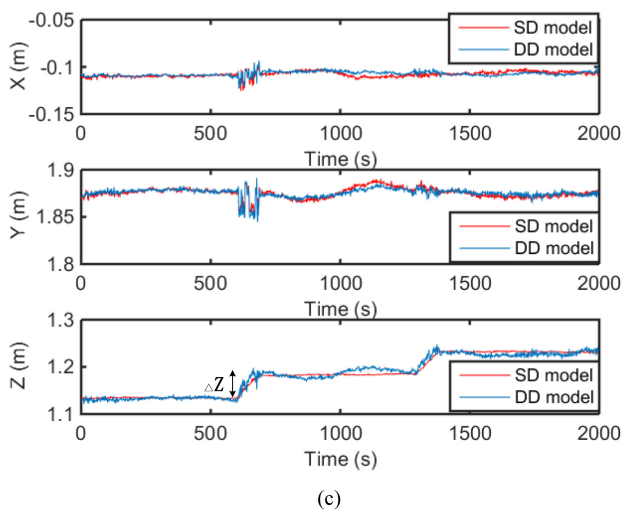
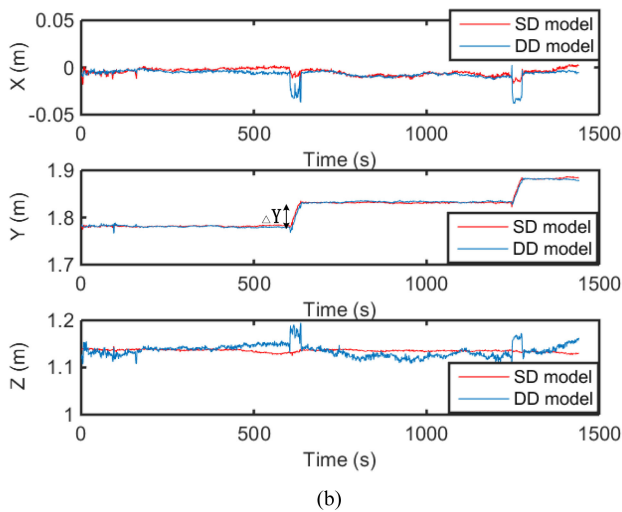
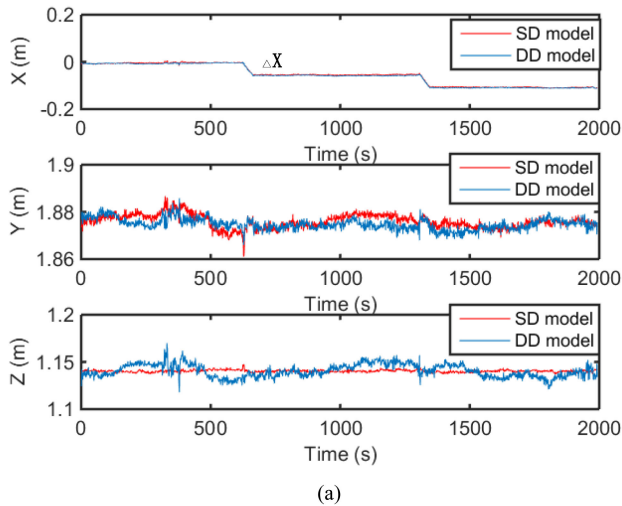


Fig. 10. Baseline measurement results of the conventional DD model and the SD model. (a) The measurements of the device moving along the x-axis. (b) The measurements of the device moving along the y-axis. (c) The measurements of the device moving along the z-axis.

IV. CONCLUSION

A multi-antenna GNSS-over-fiber system with a line bias monitoring module has been proposed for high accuracy 3D baseline measurement. In the proposed system, an external-modulation based APL was used for stable long-distance transmission of the GNSS signals. To improve the vertical precision, the carrier phase SD algorithm with microwave-photonics-based line bias compensation was used instead of the carrier phase DD algorithm. Outdoor measurement results demonstrated that an over-3-time improvement in the vertical positioning precision was achieved. The proposed method can be potentially applied for the measurement of the attitude of vehicles and the monitoring of the healthy condition of structures.

REFERENCES

- [1] L. Hu, X. Yue, and B. Ning, "Development of the Beidou ionospheric observation network in China for space weather monitoring," *Space Weather*, vol. 15, no. 8, pp. 974–984, 2017.
- [2] N. Rodriguez-Alvarez *et al.*, "Land geophysical parameters retrieval using the interference pattern GNSS-R technique," *IEEE Trans. Geosci. Remote Sens.*, vol. 49, no. 1, pp. 71–84, Jan. 2011.
- [3] J. Douša, M. Eliaš, P. Václavovic, K. Eben, and P. Krč, "A two-stage tropospheric correction model combining data from GNSS and numerical weather model," *GPS Solutions*, vol. 22, no. 3, pp. 77–89, 2018.
- [4] J. Wang, L. Xu, X. Li, and Z. Quan, "Quantitatively evaluating random attitude measurement errors' impacts on DSM elevation accuracy from Airborne Laser Scanning," *IEEE Trans. Instrum. Meas.*, vol. 62, no. 11, pp. 3101–3109, Nov. 2013.
- [5] S. T. Goh and K.-S. Low, "Survey of global-positioning-system-based attitude determination algorithms," *J. Guid. Control Dyn.*, vol. 40, no. 6, pp. 1321–1335, 2017.
- [6] Q. S. Chen *et al.*, "Vertical deformation monitoring of the suspension bridge tower using GNSS: A case study of the Forth Road Bridge in the UK," *Remote Sens.*, vol. 10, no. 3, pp. 364–382, 2018.
- [7] M. R. Kaloop, C. O. Yigit, and J. W. Hu, "Analysis of the dynamic behavior of structures using the high-rate GNSS-PPP method combined with a wavelet-neural model: Numerical simulation and experimental tests," *Adv. Space Res.*, vol. 61, no. 6, pp. 1512–1524, 2018.
- [8] T. H. Yi, H. N. Li, and M. Gu, "Recent research and applications of GPS-based monitoring technology for high-rise structures," *Struct. Control Health Monit.*, vol. 20, no. 5, pp. 649–670, 2013.
- [9] M. R. Kaloop and H. Li, "Multi input-single output models identification of tower bridge movements using GPS monitoring system," *Measurement*, vol. 47, no. 1, pp. 531–539, 2014.
- [10] R. Tu, J. H. Liu, C. X. Lu, R. Zhang, P. F. Zhang, and X. C. Lu, "Cooperating the BDS, GPS, GLONASS and strong-motion observations for real-time deformation monitoring," *Geophys. J. Int.*, vol. 209, no. 3, pp. 1408–1417, 2017.
- [11] Y. Q. Chen, X. L. Ding, D. F. Huang, and J. J. Zhu, "A multi-antenna GPS system for local area deformation monitoring," *Earth Planets Space*, vol. 52, no. 10, pp. 873–876, 2000.
- [12] R. Santerre, A. Geiger, and S. Banville, "Geometry of GPS dilution of precision: revisited," *GPS Solutions*, vol. 21, no. 4, pp. 1747–1763, 2017.
- [13] J. M. B. Oliveira, L. M. Pessoa, H. M. Salgado, G. Proudley, D. Charlton, and H. White, "Experimental evaluation of a differential GPS-over-fiber system for aircraft attitude determination," in *Proc. IEEE Avionics, Fiber-Opt. Photon. Technol. Conf.*, 2013, pp. 75–76.
- [14] L. M. Pessoa, J. M. B. Oliveira, D. Coelho, J. C. S. Castro, H. M. Salgado, and M. Fames, "Transmission of differential GPS signals over fiber for aircraft attitude determination," in *Proc. IEEE Avionics, Fiber-Opt. Photon. Dig. CD*, 2012, pp. 80–81.
- [15] W. T. Chen, H. L. Qin, Y. Z. Zhang, and T. Jin, "Accuracy assessment of single and double difference models for the single epoch GPS compass," *Adv. Space Res.*, vol. 49, no. 4, pp. 725–738, 2012.
- [16] P. J. G. Teunissen and A. Kleusberg, *GPS for Geodesy*. Berlin, Germany: Springer-Verlag, 1998.
- [17] R. Santerre and G. Beutler, "A proposed GPS method with multi-antennae and single receiver," *Bull. Géodésique*, vol. 67, no. 4, pp. 210–223, 1993.

- [18] J. H. Keong, "GPS/GLONASS attitude determination with a common clock using a single difference approach," in *Proc. ION GPS99 Conf.*, Nashville, TN, USA, 1999, pp. 14–17.
- [19] W. T. Chen and X. Q. Li, "Success rate improvement of single epoch integer least-squares estimator for the GNSS attitude/short baseline applications with common clock scheme," *Acta Geod. Geophys.*, vol. 49, no. 3, pp. 295–312, 2014.
- [20] C. E. Cohen and B. W. Parkinson, "Integer ambiguity resolution of the GPS carrier for spacecraft attitude determination," *Adv. Astronaut. Sci.*, vol. 1, pp. 107–118, 1992.
- [21] D. Macias-Valadez, R. Santerre, S. Larochelle, and R. Landry, "Improving vertical GPS precision with a GPS-over-fiber architecture and real-time relative delay calibration," *GPS Solutions*, vol. 16, no. 4, pp. 449–462, 2012.
- [22] X. Jiang, X. C. Wang, and S. L. Pan, "A multi-antenna GNSS-over-fiber system with high vertical precision," in *Proc. Int. Top. Meet. Microw. Photon.*, Toulouse, France, 2018, pp. 1–4.
- [23] G. Lachapelle, M. E. Cannon, and G. Lu, "High-precision GPS navigation with emphasis on carrier-phase ambiguity resolution," *Mar. Geodesy*, vol. 15, no. 4, pp. 253–269, 1992.
- [24] L. Zhang, Y. Q. Hou, and J. Wu, "A drift line bias estimator: ARMA-based filter or calibration method, and its application in BDS/GPS-based attitude determination," *J. Geodesy*, vol. 90, no. 12, pp. 1331–1343, 2016.
- [25] P. J. G. Teunissen, "The Lambda Method for the GNSS Compass," *Artif. Satell.*, vol. 41, no. 3, pp. 89–103, 2006.
- [26] K. M. Abadir and J. R. Magnus, *Matrix Algebra*. Cambridge, U.K.: Cambridge Univ. Press, 2005.
- [27] C. H. Cox, G. E. Betts, and L. M. Johnson, "An analytic and experimental comparison of direct and external modulation in analog fiber-optic links," *IEEE Trans. Microw. Theory Techn.*, vol. 38, no. 5, pp. 501–509, May 1990.
- [28] D. A. I. Marpaung, "High dynamic range analog photonic links: Design and implementation," Ph.D. dissertation, Faculty Elect. Eng., Math. Comput. Sci., Univ. Twente, Enschede, The Netherlands, 2009.

Xin Jiang received the B.S. degree in information engineering from the Nanjing University of Aeronautics and Astronautics, Nanjing, China, in 2014, and the B.S. degree in radio engineering from the National University of Aeronautics and Astronautics of Zukovsky, Zukovsky, Ukraine, in 2014. He received the M.S. degree in navigation guidance and control in 2007 from the Nanjing University of Aeronautics and Astronautics, where he is currently working toward the Ph.D. degree in communication and information system. His research interests include GNSS application in engineering, photonic microwave measurement, and photonic technologies for signal processing.

Xiangchuan Wang received the B.Eng. degree in automation and the Ph.D. degree in microelectronics and solid-state electronics from Nanjing University, Nanjing, China, in 2009 and 2015, respectively. He is currently a Lecturer with the Key Laboratory of Radar Imaging and Microwave Photonics, Ministry of Education, Nanjing University of Aeronautics and Astronautics, Nanjing, China. His current research interests include microwave photonic measurement and optical fiber sensing technologies.

Angran Zhao received the B.S. degree in communication engineering from Xi'an University of Posts and Telecommunications, Xi'an, China, in 2015. He is currently working toward the M.S. degree with the Key Laboratory of Radar Imaging and Microwave Photonics, Ministry of Education, Nanjing University of Aeronautics and Astronautics, Nanjing, China. His research interests include high dynamic range analog photonic links and photonics-based imaging radar.

Jianping Yao (M'99–SM'01–F'12) received the Ph.D. degree in electrical engineering from the Université de Toulon et du Var, Toulon, France, in December 1997. He is a Distinguished University Professor and University Research Chair with the School of Electrical Engineering and Computer Science, University of Ottawa, Ottawa, ON, Canada. From 1998 to 2001, he was with the School of Electrical and Electronic Engineering, Nanyang Technological University, Singapore, as an Assistant Professor. In December 2001, he joined the School of Electrical Engineering and Computer Science, University of Ottawa, as an Assistant Professor, where he was promoted to Associate Professor in May 2003,

and Full Professor in May 2006. He was appointed University Research Chair in Microwave Photonics in 2007. In June 2016, Prof. Yao was conferred the title of Distinguished University Professor of the University of Ottawa. From July 2007 to June 2010 and July 2013 to June 2016, he was Director of the Ottawa-Carleton Institute for Electrical and Computer Engineering.

He has authored or co-authored more than 580 research papers (Citations: >16,000, H-index: 64) including more than 340 papers in peer-reviewed journals and more than 240 papers in conference proceedings. He is the Editor-in-Chief of IEEE Photonics Technology Letters, a former Topical Editor of *Optics Letters*, an Associate Editor for *Science Bulletin*, a Steering Committee Member of IEEE Journal of Lightwave Technology, and an Advisory Editorial Board Member of *Optics Communications*. He was a Guest Editor of a Focus Issue on Microwave Photonics in *Optics Express* in 2013, a Lead-Editor of a Feature Issue on Microwave Photonics in *Photonics Research* in 2014, and a Guest Editor of a Special Issue on Microwave Photonics in IEEE/OSA Journal of Lightwave Technology in 2018. He is currently the Technical Committee Chair of IEEE MTT-3 Microwave Photonics and an elected member of the Board of Governors of the IEEE Photonics Society (2019–2021). He was a member of the European Research Council Consolidator Grant Panel in 2016 and 2018, the Qualitative Evaluation Panel in 2017, and a panelist of the National Science Foundation Career Awards Panel in 2016. He was also a Chair of a number of international conferences, symposia, and workshops, including the Vice Technical Program Committee (TPC) Chair of the 2007 IEEE Topical Meeting on Microwave Photonics, TPC Co-Chair of the 2009 and 2010 Asia-Pacific Microwave Photonics Conference, TPC Chair of the High-Speed and Broadband Wireless Technologies Subcommittee of the IEEE Radio Wireless Symposium 2009–2012, TPC Chair of the Microwave Photonics Subcommittee of the IEEE Photonics Society Annual Meeting 2009, TPC Chair of the 2010 IEEE Topical Meeting on Microwave Photonics, General Co-Chair of the 2011 IEEE Topical Meeting on Microwave Photonics, TPC Co-Chair of the 2014 IEEE Topical Meetings on Microwave Photonics, General Co-Chair of the 2015 and 2017 IEEE Topical Meeting on Microwave Photonics, and General Chair of the 2019 IEEE Topical Meeting on Microwave Photonics. He was also a committee member for a number of international conferences, such as IPC, OFC, CLEO, BGPP, and MWP. He received the 2005 International Creative Research Award of the University of Ottawa, the 2007 George S. Glinski Award for Excellence in Research, a Natural Sciences and Engineering Research Council of Canada Discovery Accelerator Supplements Award, the 2017–2018 Award for Excellence in Research of the University of Ottawa, and the 2018 R.A. Fessenden Silver Medal from IEEE Canada. He was selected to receive an inaugural OSA Outstanding Reviewer Award in 2012 and was one of the top ten reviewers of IEEE/OSA Journal of Lightwave Technology 2015–2016. He was an IEEE MTT-S Distinguished Microwave Lecturer for 2013–2015.

He is a registered Professional Engineer of Ontario. He is a Fellow of the Optical Society of America (OSA), the Canadian Academy of Engineering (CAE), and the Royal Society of Canada (RSC).

Shilong Pan (S'06–M'09–SM'13) received the B.S. and Ph.D. degrees in electronics engineering from Tsinghua University, Beijing, China, in 2004 and 2008, respectively. From 2008 to 2010, he was a "Vision 2010" Postdoctoral Research Fellow with the Microwave Photonics Research Laboratory, University of Ottawa, Ottawa, ON, Canada. In 2010, he joined the College of Electronic and Information Engineering, Nanjing University of Aeronautics and Astronautics, Nanjing, China, where he is currently a Full Professor and the Executive Director with the Key Laboratory of Radar Imaging and Microwave Photonics, Ministry of Education. His research focuses on microwave photonics, which includes optical generation and processing of microwave signals, analog photonic links, photonic microwave measurement, and integrated microwave photonics. He has authored or coauthored more than 420 research papers, including more than 230 papers in peer-reviewed journals and 190 papers in conference proceedings. He is currently an associate editor of *Electronics Letters*, a Topical Editor of *Chinese Optics Letters*, and is a Technical Committee member of IEEE MTT-3 Microwave Photonics. He was the recipient of an IEEE Photonics Society Distinguished Lecturer award in 2019, an OSA Outstanding Reviewer Award in 2015, a Top Reviewer of the JOURNAL OF LIGHTWAVE TECHNOLOGY in 2016 and 2018, and a Publons Peer Reviewer Award in 2018. He is a Chair of numerous international conferences and workshops, including the TPC Chair for the International Conference on Optical Communications and Networks in 2015, and the TPC Co-Chair for the IEEE INTERNATIONAL TOPICAL MEETING ON MICROWAVE PHOTONICS in 2017. He is a Fellow of SPIE and IET.